



In situ characterization of residual stress evolution during heat treatment of SiC/SiC ceramic matrix composites using high-energy X-ray diffraction

Michael W. Knauf¹  | Craig P. Przybyla² | Paul A. Shade²  | Jun-Sang Park³ | Andrew J. Ritchey⁴ | Rodney W. Trice⁵ | R. B. Pipes⁶

¹School of Aeronautics and Astronautics, Purdue University, West Lafayette, IN, USA

²Materials and Manufacturing Directorate, Air Force Research Laboratory, Wright-Patterson Air Force Base, OH, USA

³Advanced Photon Source, Argonne National Laboratory, Lemont, IL, USA

⁴Rolls-Royce Corporation, Indianapolis, IN, USA

⁵School of Materials Engineering, Purdue University, West Lafayette, IN, USA

⁶Schools of Aeronautics and Astronautics, Materials Engineering and Chemical Engineering, Purdue University, West Lafayette, IN, USA

Correspondence

Michael W. Knauf, School of Aeronautics and Astronautics, Purdue University, West Lafayette, IN 47907, USA.
Email: michael.knauf@us.af.mil

Present address

Michael W. Knauf, Arnold Air Force Base, TN 37389, USA

Funding information

Research funding provided by the US Air Force, and materials provided by Rolls Royce.

Abstract

Volumetric strains were measured in silicon carbide/silicon carbide melt-infiltrated ceramic matrix composites (CMCs) at ambient and high temperatures using high-energy synchrotron X-ray diffraction (XRD). Both silicon and silicon carbide constituents were interrogated utilizing a broad spectrum of diffracting planes that would be largely inaccessible to common laboratory XRD equipment. Residual room-temperature principal strains in the melt-infiltrated silicon phase were found to be approximately $1100 \mu\epsilon$ in compression, corresponding to stresses of approximately 300 MPa using simplifying constitutive assumptions. Residual room-temperature principal strains in silicon carbide particles found throughout the matrix were approximately $500 \mu\epsilon$ in tension, corresponding to approximately 300 MPa. Residual strains were found to decrease considerably as temperatures increased from ambient temperature to 1250°C . Residual strains returned to approximately preheat treatment values after cool-down to ambient temperature. Strain measurements in the silicon phase were found to be significantly affected by dissolved boron dopant levels causing contraction of the silicon lattice. This contraction must be accounted for in high-temperature experiments for accurate calculation of stresses in the silicon phase.

KEYWORDS

ceramic matrix composites, heat treatment, stress relaxation

1 | INTRODUCTION

Multiple studies have investigated the residual stress state of melt-infiltrated SiC/SiC ceramic matrix composites (CMCs) through the utilization of Raman spectroscopy,¹⁻⁵ the common intersection point (CIP) method,⁶⁻⁸ and surface X-ray diffraction

(XRD) techniques.⁹⁻¹¹ Raman spectroscopy is predominately a surface technique, characterizing microstresses within tens of micrometers of the free surfaces, and thus Raman spectroscopy cannot capture volumetric stresses. The CIP method investigates large specimens and determines a single volume-averaged residual stress data point per specimen, consuming relatively

This study is based upon Knauf dissertation entitled "Effects of Heat Treatment on SiC-SiC Ceramic Matrix Composites," Purdue University, 2017.

large and costly samples in the process. In contrast, others have investigated applied stresses in CMCs utilizing volumetric XRD techniques.^{12,13} Ramirez-Rico et al have shown the viability of monitoring volumetric stress in CMCs by in situ high-energy XRD in transmission geometry.¹³ By incorporating a high-temperature furnace, it is possible to use this technique to observe changes to the stress state of CMC constituents through varying temperatures. This method provides a viable option to investigate the volumetric effects of heat treatment on CMCs and validate previous work utilizing surface measurements.^{4,14} In addition, due to (a) the unique nature of silicon crystals within CMCs; (b) the multitude of silicon carbide particles often found in CMCs; (c) the many families of crystallographic planes accessible by using very short X-ray wavelengths; and (d) the extreme brilliance of X-rays found at synchrotron facilities, hundreds of data points can be acquired with a small specimen in seconds. This provides significant advantages over Raman spectroscopy, CIP, and traditional laboratory XRD methods.

Experiments were performed at beamline 1-ID at Argonne National Laboratory's Advanced Photon Source (APS) to evaluate the evolution of the residual stress state of a slurry melt-infiltrated CMC through the temperature regime of 40°C-1250°C. The goal of these tests was to understand the time and temperature residual stress dependencies of various CMC constituents and the role each constituent plays in these changes. These experiments were undertaken to determine the CMC constituent residual stress state at high temperature, and develop an understanding of relaxation and other mechanisms involved within the material at these temperatures. Utilizing powder diffraction methods, XRD signatures from both silicon and silicon carbide phases in the material were tracked throughout heat treatments.

2 | EXPERIMENTAL PROCEDURES

2.1 | Specimen description

The composite under investigation is fabricated from multiple plies of Hi-NicalonTM fibers forming a 0°/90° 5 harness satin (2D) weave, where the fiber tows have the same quantity of fibers in the warp and weft directions, and the plies were laid up without introducing off-axis orientation. The matrix was produced with a slurry melt, which consisted primarily of boron-doped silicon and small 6H α -SiC particles. The α -SiC particles consisted exclusively of the 6H polytype, verified through more than 400 individual Raman spectroscopy measurements of the microstructure.¹⁴ A representative microstructure image of the investigated matrix is shown in Figure 1.

Twenty CMC specimens, cut from the same panel, were utilized in the high-temperature in situ study. The specimen dimensions were 4 mm in the fiber weft direction, 3 mm in the fiber warp direction, and approximately 4 mm in the transverse

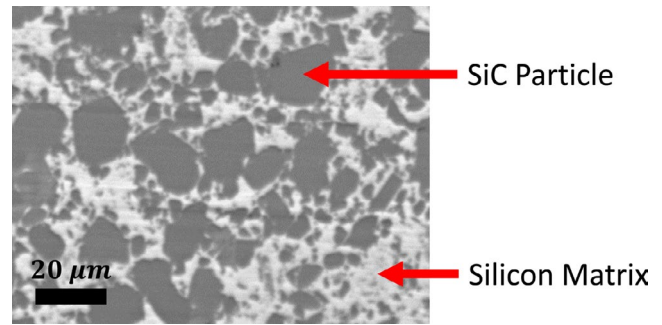


FIGURE 1 Example microstructure of investigated ceramic matrix composite. Dark gray particles are 6H silicon carbide, while light areas make up silicon matrix [Color figure can be viewed at wileyonlinelibrary.com]

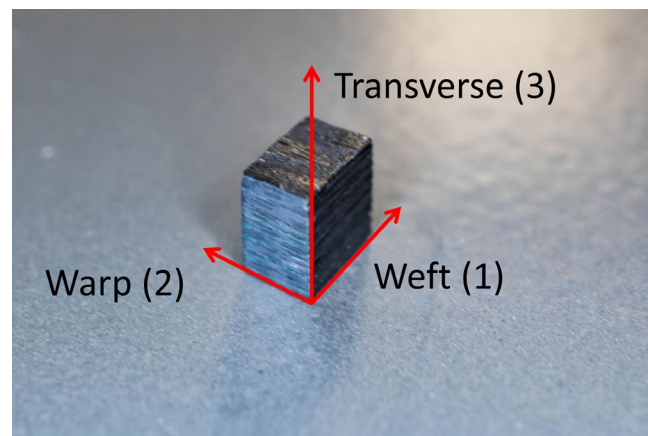


FIGURE 2 Example of in situ sample. X-ray diffraction measurements were taken parallel to the warp fiber direction in the central one-half of material [Color figure can be viewed at wileyonlinelibrary.com]

(through-thickness) direction (Figure 2). The material size was chosen to fit within the 7 mm diameter furnace utilized in the study. The specimens were randomly chosen from a batch of more than 50 samples to eliminate systematic bias and satisfy the governing assumptions of the statistics used in analysis. Additional details of the material and preparation can be found in literature.⁴

2.2 | Experimental setup

The experiments were conducted at the APS 1-ID beamline using monochromatic X-rays with an energy of 71.676 keV or wavelength of $\lambda = 0.017297$ nm. A series of slits were used to define the beam size to $200 \mu\text{m} \times 200 \mu\text{m}$. Four amorphous silicon detectors with a $0.2 \times 0.2 \text{ mm}^2$ pixel size and 2048×2048 pixels were used in a diamond array.¹⁵ Exposures were taken at a rate of approximately one every 1.3 seconds (1.2 second exposures and 0.1 second dead times), resulting in 224 exposures between four panel detectors over 5 minutes (while increasing temperature) or 44 exposures over 1 minute (while decreasing temperature).

The detector array was nominally placed at 1.33 m from the sample. Its position with respect to the sample and the direct beam was calibrated using the CeO_2 powder.¹⁶ Calibration measurements were taken at ambient conditions. Background images were taken periodically with the X-ray shutter closed; these images were subtracted from subsequent XRD images, resulting in trivial noise levels.

2.3 | Heat-treatment procedures

The specimens were cleaned and placed in a sample vacuum container for 20 days prior to testing to remove trapped air from voids prior to heat treatment. Specimens were mounted so as to direct the incident X-rays parallel to the warp fibers. In this configuration, strains in the weft and transverse directions, which are orthogonal to the incident X-ray beam, could be measured. An argon flow was introduced to the sample prior to heating at a flow rate of approximately 30 cc/min.

In situ heating was accomplished using a Linkam TS1500 heated stage (Linkam Scientific Instruments). Literature suggests that no stress relaxation in CMCs occurs at less than 900°C.^{2,3} Therefore, the first of two heating profiles (Profile A, utilized for 15/20 specimens) included an initial set of exposures for 5 minutes at 40°C, an immediate ramp to 900°C, where the temperature was held constant for 5 minutes while collecting exposures, after which the temperature ramped in 50°C increments and held at the respective temperature for 5 minutes while collecting exposures, etc. The hold temperatures were 40°C, from 900°C through 1250°C in 50°C increments, then 1200°C through 900°C in 50°C increments, and 40°C. The hold times were for 5 minutes at each temperature while increasing in temperature, and 1 minute for each temperature while decreasing in temperature. The ramp rates were 60°C/min while increasing temperature and 100°C/min while decreasing temperature. Whereas Profile A provided temperature increments for studying stresses at various heat-treatment temperatures, Profile B maximized time at 1250°C to study maximum potential effects of heat treatment. Profile B included an initial hold at 40°C, followed by a ramp to 1250°C at a rate of 60°C/min, a hold for 30 minutes, and ramp back to 40°C at a rate of 100°C/min. The total time at or above 900°C was approximately 56 minutes for Profile A, and 42 minutes for Profile B. Both profiles can be found in Figure 3.

3 | ANALYSIS METHODOLOGY

3.1 | Utilizing XRD to measure strain state

Incident X-rays transmitted through a powder of crystalline material produce Debye-Scherrer diffraction cones. These

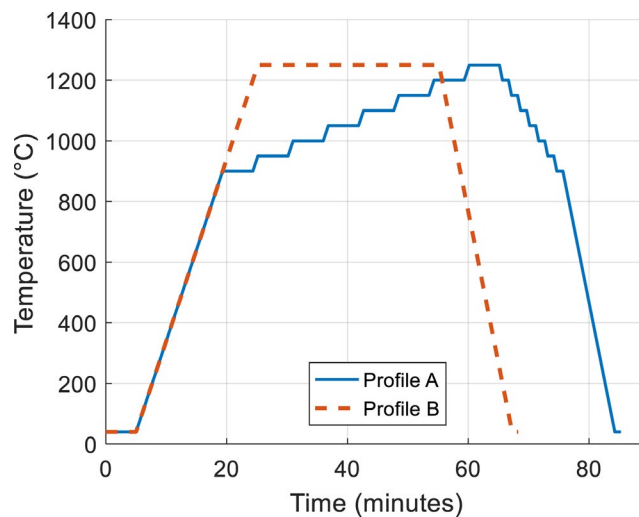


FIGURE 3 Temperature schedules for Profiles A (15/20 specimens) and B (5/20 specimens). Profile A provided greater temperature discrimination, while Profile B provided significantly greater time at the highest heat-treatment temperature of 1250°C [Color figure can be viewed at wileyonlinelibrary.com]

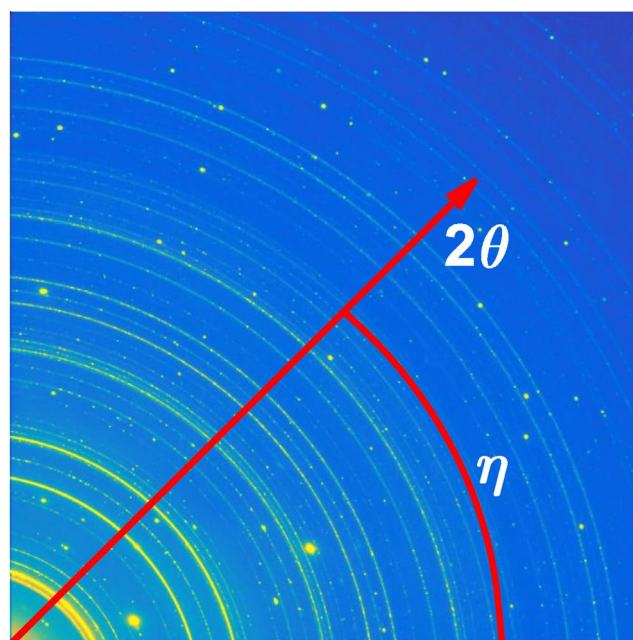


FIGURE 4 Example X-ray diffraction pattern, as produced through this research. Continuous rings are representative of a distribution of small randomly oriented silicon carbide particles, while single spots represent individual silicon crystals each with a particular orientation. The angle 2θ is shown as the radial distance from the pattern center to the diffraction peak on the detector (changes of which are utilized to determine strain), while the azimuth (η) is the beam axis starting from an arbitrary origin (the horizon in the present case) [Color figure can be viewed at wileyonlinelibrary.com]

diffraction cones can be captured using an area detector. The resulting diffraction patterns can be used to extract microstructure and state information of the powder.¹⁷ Figure 4 illustrates a

typical diffraction pattern acquired from the APS Hydra detector array. Diffraction is governed by Bragg's law (Equation 1):

$$2d_{hkl}\sin(\theta_{hkl}) = \lambda, \quad (1)$$

where λ is the X-ray wavelength, d_{hkl} is the plane spacing for the family of crystallographic planes, hkl , and θ_{hkl} is the corresponding Bragg angle. In our experiment, we used monochromatic X-rays to measure the change in θ_{hkl} as a function of azimuthal angle (η) and temperature (T), as illustrated in Figure 4. The change in Bragg angle from a reference condition is used to measure the lattice strain, ϵ , through Equation 1:

$$\epsilon = \frac{\sin(\theta_0)}{\sin(\theta)} - 1, \quad (2)$$

where θ_0 is the Bragg angle measured at the reference state of the phase and θ is the Bragg angle of the phase in a deformed state. In our case, the reference θ_0 was measured using stress-free powder forms of the SiC particulate and silicon matrix materials at room temperature.

3.2 | Accounting for thermal expansion

The slurry melt CMC production process used to manufacture the investigated specimens includes a chemical vapor infiltration (CVI) coating on the fiber preform, followed by a slurry infiltration, and finally a silicon-alloy melt infiltration step. These processes inherently generate various residual stresses on material constituents. A particularly important source of residual stress is due to a mismatch of constituent coefficients of thermal expansion (CTE).

As the temperature of a composite changes, the composite and its constituents will naturally grow or shrink due to thermal expansion. Although free thermal expansion in homogenous materials produces no stress, the constituents within a composite are mechanically constrained and are thus unable to freely expand, producing a residual stress at temperatures which differ from the stress-free temperature. In addition, the stress-free temperature for each major constituent is likely different due to the multiple steps involved within the manufacturing process.¹⁸ As temperatures vary from the temperature at which the stress-free materials were referenced in Equation (2), the change in overall lattice strain will be affected by both thermal growth and a mechanical constraint within the composite between the various constituents (ie, residual strain). Equation (3) accounts for thermal growth and decomposes residual strain from strain induced by otherwise free thermal expansion by utilizing the particular constituent CTE. These effects are combined:

$$\epsilon_{i,Res} = \epsilon_{i,T_1} - \int_{T_0}^{T_1} \alpha(T)dT, \quad (3)$$

where $\epsilon_{i,Res}$ is the computed residual strain state, ϵ_{i,T_1} is the measured strain state at high temperature, and $\alpha(T)$ is the CTE as a function of temperature, evaluated from a reference temperature, T_0 , to the temperature of interest, T_1 .

3.3 | Strain to stress conversion

Low-energy X-rays generally do not penetrate more than a few hundred nanometers into the probed material, providing validity for plane stress assumptions typically employed in determining the state of stress within the material.¹⁹ High-energy X-rays (50 keV+) have large penetration depths²⁰ and allow transmission geometry to be utilized. In this case, X-rays interrogate the entire illuminated volume and using the plane stress assumption is not appropriate in converting the measured strains to stresses. With area detectors, both the weft (1) and transverse (3) strains (in fact, all strains in the 1-3 plane) can be measured simultaneously, while the warp (2) direction parallel to the incident beam is unattainable without sample rotation. In addition, rotation is impossible with the current laboratory setup due to furnace geometry. Simplifying assumptions are necessary to convert the two attainable strains into a three-dimensional stress tensor.

Due to the small particle size relative to the X-ray beam size and the random crystal orientations that are generated by the production process, the aggregate of polycrystalline constituents is readily modeled as isotropic materials when averaged over the large (relative to the constituents) X-ray spot size (200 $\mu\text{m} \times 200 \mu\text{m}$). Simplifying the material properties for isotropic assumptions requires both Poisson's ratios and Young's moduli of measured constituents. To account for thermal growth of constituents through heat treatment, the constituent CTE as a function of temperature must also be employed.

Being an orthotropic composite, when taken as a whole, the residual strains within the bulk of the composite in the two fiber directions should be approximately equal. We can then assume that the average value of strain (represented by an overbar) in the two fiber directions is approximately equal when thermally loaded, as is the case for all measurements made in this study. Therefore, is assumed to be approximately equal to $\bar{\epsilon}_2$ ($\bar{\epsilon}_1 \approx \bar{\epsilon}_2$) and is used in its place in the stress formulation, as weft (2) directional strains were unattainable, as mentioned previously.

When calculating the stress parallel to either the fiber or transverse directions, the individual principal strains measured in each direction can be utilized to determine individual principal stresses per diffraction peak in the respective investigated direction. However, due to the small crystal sizes relative to beam size, it is extremely unlikely that a given measurement in one principal direction will correspond to the same crystal's XRD signature in the second measured principal direction. To determine the stress in the weft direction, all measured strains from all crystallographic planes in the transverse (3) direction

were numerically averaged (designated with an over bar, ie, $\bar{\epsilon}_3$) to estimate the contributions of the Poisson's effect in the off-diagonal term of the stiffness matrix (C_{12}). A similar operation was performed for the weft direction ($\bar{\epsilon}_1$) in order to calculate transverse stresses. This is demonstrated as Equations (4) and (5) are utilized to determine the principal stresses according to each point measurement, again assuming isotropic elasticity.

$$\sigma_1 = C_{11}\epsilon_1 + C_{12}\epsilon_2 + C_{12}\epsilon_3 \approx C_{11}\bar{\epsilon}_1 + C_{12}\bar{\epsilon}_1 + C_{12}\bar{\epsilon}_3, \quad (4)$$

$$\sigma_3 = C_{12}\epsilon_1 + C_{12}\epsilon_2 + C_{11}\epsilon_3 \approx C_{12}\bar{\epsilon}_1 + C_{12}\bar{\epsilon}_1 + C_{11}\epsilon_3. \quad (5)$$

Stiffness matrix terms C_{11} and C_{12} are readily calculated using Equation (6). Thus, by measuring the strains in one of the fiber directions as well as the transverse direction, the general stress state of the material can be inferred. This relationship will be used in subsequent analyses for the silicon and silicon carbide constituents.

$$C_{11} = \frac{(1-\nu)E}{(1+\nu)(1-2\nu)} \quad (6)$$

$$C_{12} = \frac{\nu E}{(1+\nu)(1-2\nu)}.$$

3.4 | Temperature-dependent silicon carbide particle properties

Munro²¹ compiled ultrasonic and resonance elastic moduli data of hexagonal 6H α -SiC (the same SiC polytype as found in the investigated CMC) as a function of temperature and determined the temperature-dependent isotropic elastic modulus and Poisson's ratio given by Equations (7) and (8), respectively, where T is in Kelvin.

$$E(T) = 415 - 0.023(T - 273) \text{ [GPa]}, \quad (7)$$

$$\nu(T) = 0.160 - 2.62 \times 10^{-6}(T - 273). \quad (8)$$

The volume-averaged CTE of randomly oriented hexagonal crystals, $\bar{\alpha}$, can be described by Equation (9), where α_a is the CTE perpendicular to the longitudinal axis and α_c is the CTE parallel to the longitudinal axis.²² Li and Bradt²³ determined the CTE for the 6H α -SiC polytype by tracking the (213), (219), and (306) XRD peaks in the a and c directions over a temperature range between 293 K and 1273 K. Combining their data with that of Inoue and Kurachi,²⁴ they developed a second-order polynomial describing the CTE over the temperature range of 293 K to 2373 K. Combining their results with Equation (9), the 6H poly-SiC temperature-dependent CTE is calculated in Equation (10).

$$\bar{\alpha} = \frac{1}{3}(2\alpha_a + \alpha_c), \quad (9)$$

$$\bar{\alpha}_{\text{SiC}}(T) = 3.37 \times 10^{-6} + 2.25 \times 10^{-9}(T - 273) - 5.61 \times 10^{-13}(T - 273)^2 \text{ [K}^{-1}\text{]}. \quad (10)$$

3.5 | Temperature-dependent silicon matrix properties

The polycrystalline silicon Poisson's ratio is taken to be $\nu_{\text{poly}} = 0.22$ at all investigated temperatures.²⁵ The modulus of elasticity for silicon is anisotropic and is dependent upon crystal orientation and temperature.²⁶ Swarnakar et al measured the Young's moduli of silicon in the $\langle 100 \rangle$, $\langle 110 \rangle$, and $\langle 111 \rangle$ crystal directions as a function of temperature and fit these to second-order polynomials.²⁷ The $\langle 110 \rangle$ and $\langle 111 \rangle$ constitutive relations are not independent, and thus the three independent stiffness coefficients cannot be determined. However, the s_{11} compliance term was determined through their work, as well as the quantity, $s_{12} + s_{44}/2$. Oftentimes, a Reuss approximation is used as the average elastic modulus of polycrystalline silicon.²⁵ These two quantities are sufficient to determine the Reuss approximation of the polycrystalline elastic modulus as a function of temperature, and will be used here as an approximation of isotropic elasticity for the polycrystalline silicon aggregate. This relationship is given by Equation (11) (after simplification) for a diamond cubic crystal (eg, silicon), where T is measured in Kelvin.²⁵ This temperature dependence results in an approximate 10% decrease in the moduli between room temperature and 1523 K, in line with the work of Ono et al.²⁶

$$E_R(T) = \frac{5}{3s_{11} + 2\left(s_{12} + \frac{s_{44}}{2}\right)} \quad (11)$$

$$= \frac{2.912 \times 10^9}{T^2 + 59.41T + 1.897 \times 10^7} \text{ [GPa]}.$$

Okada and Tokumaru²⁸ used XRD to measure the lattice parameter of silicon as a function of temperature from 300 K to 1500 K. This relationship is found in Equation (12). Although crystalline silicon is elastically anisotropic, as a material with cubic crystal symmetry, it is thermally isotropic and strains uniformly in all directions with increasing temperature.²⁵

$$\alpha_{\text{Si}}(T) = (3.725 \times (1 - \exp(-5.88 \times 10^{-3}(T - 124))) + 5.548 \times 10^{-4}T) \times 10^{-6} \text{ [K}^{-1}\text{]}. \quad (12)$$

3.6 | Dilatational effects observed in XRD due to impurities in silicon matrix

The silicon matrix utilized in this study was manufactured with a small amount of boron, a common additive in the silicon melt of CMCs.^{4,29} Impurities found within a crystal lattice of any covalently bonded material will strain the lattice in a hydrostatic manner. If the covalent radius of an impurity

is larger than that of silicon, the lattice will expand to allow more room for the larger atom. Conversely, if the impurity atom has a smaller covalent radius than silicon (such as boron), the lattice will contract. For substitutional impurities, the change in lattice parameter follows Vegard's law for small quantities of impurities,³⁰ given by Equation (13).

$$\frac{\Delta a}{a} = \beta N_i = \epsilon. \quad (13)$$

For a cubic crystal system (eg, silicon), a is the lattice spacing of the crystal, Δa is the change in the spacing due to the impurities, N_i is the concentration of impurity atoms (typically in atoms/cm³), and β is a function of the covalent radii of the two atoms and concentration of solvent atoms.³¹ This ratio of the change of length of the crystal lattice spacing to the original length is a strain on the crystal structure, and, as such, is indistinguishable from mechanical or thermal strain when measured via XRD. Vegard's law has been shown to be accurate within the silicon-boron system having boron concentrations between at least 2.5×10^{17} atoms/cm³ and 1×10^{20} atoms/cm³. For boron-doped silicon crystals within these limits, the theoretical value of $\beta = -5.46 \times 10^{-24}$ cm³/atoms, in line with experimental values.³¹⁻³³ These calculations are for substitutional boron only. If the impurities are instead interstitial atoms within the silicon lattice or if impurities precipitate out of the solid solution, the lattice parameter predictions become much more complicated and Vegard's law may no longer hold.³⁴

A temperature-dependent boron-silicon solubility relationship is therefore required for accurate high-temperature residual strain measurements, as the number of boron atoms dissolved in silicon increases with temperature if a source with sufficient boron atoms is available. Armigliato et al determined the maximum solubility of boron in silicon at temperatures between 1173 K and 1598 K.³⁵ The solubility curve follows an Arrhenius dependence, according to Equation (14). Here, $N_B(T)$ is the concentration of boron atoms dissolved in the silicon solid solution as a function of temperature, $A = 9.25 \times 10^{22}$ atoms/cm³, $E = 0.73$ eV/K, k is the Boltzmann constant ($k = 8.617 \times 10^{-5}$ eV/K), and T is the temperature in Kelvin. According to this relationship, at 1173 K, the solubility of boron in silicon is approximately 0.1%, while it is more than 0.9% at 1598 K.

$$N_B(T) = A \exp\left(-\frac{E}{kT}\right) [\text{atoms/cm}^3]. \quad (14)$$

Taken in conjunction with Vegard's law (Equation 13), an expected change in strain due to substitutional boron diffusing into the silicon lattice is given by Equation (15), assuming a boron source is available. Equations (14) and (15) are illustrated in Figure 5. As the temperature is increased,

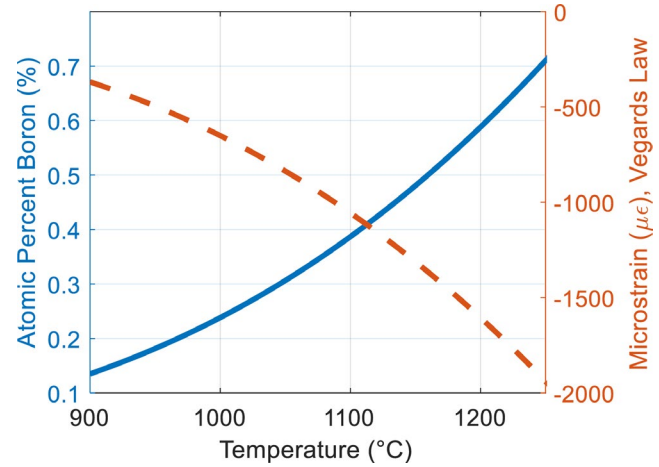


FIGURE 5 Substitutional boron percentage (left, solid line) and accompanying lattice strain (right, dotted line) as function of temperature. Apparent strain increases in magnitude dramatically as the percentage of boron increases within the silicon-boron system [Color figure can be viewed at wileyonlinelibrary.com]

more boron is allowed into the lattice, effectively reducing the lattice parameter due to the relatively small boron atoms occupying substitutional sites. This in turn affects the diffraction patterns of the silicon and appears in the analysis as a compressive strain.

$$\epsilon_{\text{Vegard}}(T) = -0.5051 \times \exp\left(-\frac{0.73}{8.617 \times 10^{-5} T}\right). \quad (15)$$

3.7 | Data collection and analysis

The XRD data collected by each of the four panels were saved as an image file, with each pixel recording a specific intensity value imparted by the Debye-Scherrer rings incident upon the panel. The four-detector panel setup allows the utilization of a larger sample-to-detector distance for the same reciprocal space coverage, thus improving strain resolution. The panel data were then converted from polar to Cartesian coordinates to facilitate analysis. As the panels produce two-dimensional data, silicon carbide particle intensities were integrated over an arc of $\pm 5^\circ$, centered on the principal (horizontal and vertical) directions. Nine 6H α -silicon carbide peaks were tracked at room- and elevated temperatures along principal directions. These nine peaks are included in Table 1 (2θ and d_{hkl} values given at room temperature, $a = 3.081$ Å, $c = 15.12$ Å). It should be noted that the other source of silicon carbide in the CMC, Hi-NicalonTM fiber, contains β -SiC and is absent of α -SiC. The β -SiC polytype produces far fewer XRD signatures. Therefore, α -SiC particle strains are calculated by choosing XRD peaks only associated with the α -SiC particles embedded within the matrix.

Utilizing area detectors instead of line or point detectors, the effect of large silicon grain size in the matrix (illustrated in Figure 4 as intense spots) can be partially negated by selecting areas of high intensity and integrating over a very small azimuth around the increased intensity. This methodology was utilized to search for high-intensity silicon peaks within $\pm 5^\circ$ of the principal directions, given the peak met a threshold value. The highest intensity peaks were then integrated over a $\pm 1^\circ$ azimuth, thus allowing the peaks which would otherwise be faint over the normal 10° integrated azimuth range appear stronger due to the selective process. By performing the analysis in this way, hundreds of individual silicon crystals were effectively tracked by using 11 X-ray *hkl* planes, found in Table 2.

A nonlinear least squares MATLAB routine was utilized to fit the diffraction data to pseudo-Voigt functions in conjunction with linear backgrounds. An example of a fit is shown in Figure 6 for diffraction data acquired at 40°C . The peak under investigation is an intense {422} silicon peak at 8.97° . Houk et al recommend bounds of approximately five times the full width at half maximum of the fitted peak.³⁶ Because an α -SiC peak {208} is also within these bounds at approximately 9.11° , both were fitted, along with a linear baseline.

4 | RESULTS AND DISCUSSION

4.1 | Silicon carbide particle strain state due to heat treatment

Utilizing the 20 tested specimens and the multiple peaks found in Table 1, more than 300 measurements were recorded for SiC particles in both principal directions before and after heat treatment at 1250°C . These measurements exhibited normal distributions. The average SiC particle residual strain in the weft fiber (1) direction at 40°C prior to heat treatment was $480 \mu\epsilon$, while the average strain in the fiber direction after the heat treatment was complete was $440 \mu\epsilon$, a decrease of $40 \mu\epsilon$. The average strain in the transverse (3) direction at 40°C prior to heat treatment was $530 \mu\epsilon$, while the average strain in the transverse direction after the heat treatment was complete was $540 \mu\epsilon$, an increase of approximately $10 \mu\epsilon$. Given that the resolution of the experimental setup is approximately $50 \mu\epsilon$, these changes in strain are negligible. A *t* test was performed on the datasets to determine if there was a statistically significant change due to heat treatment; no such statistically relevant change was observed, as evidenced by the large *P*-values found in Table 3.

Additionally, there was no appreciable difference between the results of either heating profile.

4.2 | Silicon matrix strain state due to heat treatment

Utilizing the 11 *hkl* planes for silicon referenced in Table 2, more than 400 silicon peaks were tracked throughout heat treatment. Strains in the fiber and transverse directions were compared before and after heat treatments. No significant difference was observed between either heating profiles, and thus results from both profiles are combined. Silicon matrix strains displayed normal distributions similar to those of silicon carbide particles. The average strain in the fiber weft (1) direction prior to heat treatment was measured as $-1180 \mu\epsilon$, while after the heat treatment, the strain relaxed to $-1080 \mu\epsilon$, a relaxation of approximately $100 \mu\epsilon$. The average strain in the transverse (3) direction prior to heat treatment was measured as $-1020 \mu\epsilon$, while after the heat treatment, the strain changed to approximately $-1050 \mu\epsilon$, an increase in the magnitude of compressive strain of approximately $30 \mu\epsilon$. Two-sample *t* tests were utilized to determine the statistical differences found through heat treatments. The *t* tests demonstrate that any affects due to heat treatment are likely minimal, with relatively high *P*-values. Additionally, both the strain in SiC particles and the strain in silicon in the fiber direction seemed to relax, signifying that there may be a correlation between heat treatments at 1250°C and the strain state relaxing within the material. However, if there is a relaxation of residual strains and stresses occurring at these levels, it is likely a relatively small percentage of the overall strain state. All results comparing strains before and after heat treatment can be found in Table 3.

4.3 | Strain state of silicon carbide particles as a function of temperature

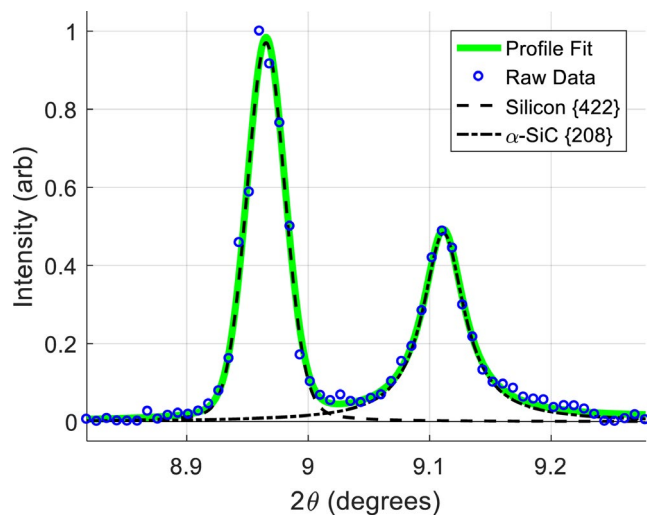
X-ray diffraction data were taken in situ at high temperatures between 900°C and 1250°C in 50°C increments to capture temperature-induced relaxation. Utilizing the same nine SiC peaks as before, the strain state is captured and reveals a steadily increasing absolute strain within the SiC throughout the heat treatment. This is an expected result of

TABLE 1 Tracked α -SiC *hkl* planes, nominal/reference 2θ values, and interplanar spacing (*d*-spacing)

<i>hkl</i>	105	107	109	205	207	216	308	228	319
$2\theta(^{\circ})$	4.956	5.907	6.977	8.127	8.741	10.60	12.34	13.93	14.68
$d_{\text{A}}(\text{\AA})$	2.000	1.679	1.421	1.220	1.135	0.9362	0.8046	0.7132	0.6771

TABLE 2 Tracked silicon hkl planes, nominal/reference 2θ values, and interplanar spacing (d -spacing)

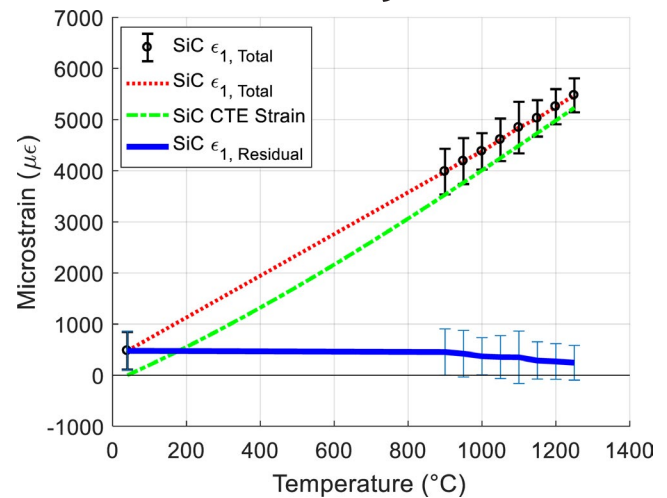
hkl	220	311	422	531	620	551
$2\theta(^{\circ})$	5.163	6.055	8.949	10.81	11.56	13.03
$d_A(\text{\AA})$	1.92	1.638	1.109	0.918	0.859	0.76
hkl	642	553	660	555	931	
$2\theta(^{\circ})$	13.69	14.05	15.53	15.85	17.48	
$d_A(\text{\AA})$	0.726	0.707	0.64	0.627	0.569	

**FIGURE 6** Example profile fit of silicon {422} peak at 8.97° and α -SiC {208} peak at 9.11° , fitted with two pseudo-Voigt functions. The small open circles indicate normalized raw data, while the various dashed lines provide the two pseudo-Voigt fits. The thick solid line indicates the overall fit [Color figure can be viewed at wileyonlinelibrary.com]**TABLE 3** As-received (AR) and heat-treated (HT) strains and standard deviations for SiC particles and silicon crystallites

	Prior to heat treatment ($\mu\epsilon$)	Post heat treatment ($\mu\epsilon$)	P -value for $\epsilon_{AR} \neq \epsilon_{HT}$
Mean ϵ_1 (SiC)	480 ± 370	440 ± 360	0.18
Mean ϵ_3 (SiC)	530 ± 320	540 ± 350	0.71
Mean ϵ_1 (silicon)	-1180 ± 710	-1080 ± 800	0.17
Mean ϵ_3 (silicon)	-1020 ± 750	-1050 ± 780	0.66

the particles (and entire composite sample, expanding with temperature.

Results of this analysis are shown in Figure 7 for the fiber weft direction. The transverse direction provided similar results. The measured strains are shown at the temperatures studied as open circles with error bars designating the standard deviation. Differences in strain state before and after

**FIGURE 7** Silicon carbide particle strain state ϵ_1 in fiber weft direction through heat treatment is shown by open circles, with error bars denoting strain standard deviation. The dashed coefficients of thermal expansion (CTE) strain line represents expected strain due to thermal expansion effects as a function of temperature. The solid $\epsilon_{1,Residual}$ line represents the difference of these two, equaling the residual strain in silicon carbide as a function of temperature. The published CTE measurement standard deviations²³ were combined with those of the X-ray diffraction measurements through the square root of the sum of their squares and these combined standard deviations are displayed on the SiC $\epsilon_{1,Residual}$ line. Silicon carbide strain states returned to approximately the same preheat treatment levels following heat treatment. All lines are guides to the eye [Color figure can be viewed at wileyonlinelibrary.com]

heat treatment at the various measured temperatures are imperceptible on this scale; strains measured while decreasing temperature were essentially equal to strains measured while increasing temperature. The dashed line beginning at $0 \mu\epsilon$ at 40°C represents stress-free silicon carbide strain as a function of temperature. The thick, nearly horizontal line beginning at $480 \mu\epsilon$ at 40°C denotes the change in residual strain with temperature, according to Equations (3) and (10). The manufacturing temperature, or the temperature at which strains began developing within the silicon carbide particles, is assumed to be approximately 1414°C (the temperature at which silicon melts³⁷), and thus it is an expected result that the residual strains diminish as temperatures approach manufacturing temperatures. This plot demonstrates that the residual strain of SiC particles in the fiber direction diminishes from an average value of approximately $480 \mu\epsilon$ to a value of approximately $200 \mu\epsilon$ at 1250°C . The residual strain in the transverse direction diminishes from an average value of approximately $530 \mu\epsilon$ to a value of approximately $270 \mu\epsilon$ at 1250°C .

Additionally, the constitutive relationships of Equations (4)-(8) were utilized to generate the residual stress information found in Table 4. At 40°C , mean SiC principal stresses in the fiber direction are approximately 290 MPa. The

transverse stresses were similar, around 310 MPa. Assuming that the warp (2) direction stresses are similar to the weft (1) direction stresses, the residual stress state is found to be relatively isotropic. These low-temperature stresses are comparable to those found through Raman spectroscopy studies.⁴ The high-temperature residual stresses decrease with increasing temperature through data taken at 1250°C. At this temperature, mean stresses in the fiber direction are approximately 120 MPa, while mean stresses in the transverse direction are approximately 150 MPa. However, the nominal strain (and stress) state returns to its former level, within machine resolution as discussed above, after the material is cooled back down to 40°C.

An ANOVA was performed on the total SiC strain at assessed temperatures and determined that the changes displayed in the total strain data shown in Figure 7 are statistically significant with an exceptionally low P -value. Between 245 and 324 individual SiC measurements were utilized in the analysis, providing a high degree of certainty in the subsequent results. Although the standard deviations are large, pairwise statistical tests between the multitude of measured strains at each temperature show a statistically significant change in total strain for each comparison at the $P < .05$ significance level. The maximum calculated P -value was .018, found through comparing strains at 1100°C and 1150°C. All other comparisons have $P < .01$. Therefore, although standard deviations are large, we can say with high confidence that the total strain shows temperature dependence.

A follow-on ANOVA was performed on the residual strains at the measured temperatures, again resulting in extremely low p -values, which demonstrate strain temperature dependence. When performing pairwise comparisons, residual strains at adjacent 50°C temperatures showed no statistically significant changes. For example, the mean residual strain at 1000°C for SiC is 370 $\mu\epsilon$, while at 1050°C it is 355 $\mu\epsilon$. However, when the residual strain at 1000°C is compared to that at 1250°C (244 $\mu\epsilon$), the statistics show that there

is significant difference ($P = .016$). This trend continued for all strain comparisons at or above 900°C with temperature differences of at least 250°C. Pairwise strain comparisons between 40°C and 1000°C and greater also differed at statistically relevant levels. Therefore, although the data certainly have too much variability to show each mean is different, it does have the power to demonstrate the trend is correct.

4.4 | Strain state of silicon as a function of temperature

Figure 8 displays the average ϵ_1 strains measured in silicon as a function of temperature. The measured strains are shown at the various elevated temperatures, with error bars designating the standard deviation between measured points at the respective temperatures. The thick solid line denotes the change in silicon strain with temperature after accounting for thermal expansion, using Equation (3) in conjunction with the silicon CTE data of Equation (12). Expected thermal expansion strain is shown as the dotted line beginning at 0 $\mu\epsilon$ at 40°C. The thermal loading and unloading data are nearly identical, and are thus not differentiated within this plot, demonstrating very little effect of the final heat-treatment temperature of 1250°C on the silicon residual strain state.

Unlike the profiles for silicon carbide in which the residual strains relaxed with increasing temperature, these profiles show a continual increase in the magnitude of the compressive strain with increasing temperature in both the fiber and transverse directions. However, as discussed previously, an increase in the amount of dissolved boron within the silicon matrix will manifest as an otherwise unexpected decrease in lattice parameter (ie, strain). Without accounting for boron solubility, this increase in compressive strain is an otherwise unexpected result, as the strains should be relaxing in a similar manner to the strains found in silicon carbide. At high temperatures, the solubility of boron in silicon increases

TABLE 4 SiC particle and silicon matrix residual stresses through heat treatment. Presented silicon stresses utilize the Vegard's law correction, assuming boron solubility is maximized, and thus is possibly overestimating the actual residual stress at high temperatures

Temperature (°C)	Mean SiC σ_1 (MPa)	Mean SiC σ_3 (MPa)	Mean Silicon σ_1 (MPa)	Mean Silicon σ_3 (MPa)
40	290 ± 160	310 ± 150	-290 ± 150	-280 ± 150
900	260 ± 180	270 ± 140	-210 ± 140	-230 ± 170
950	230 ± 190	250 ± 150	-190 ± 150	-200 ± 150
1000	210 ± 160	240 ± 140	-160 ± 140	-170 ± 150
1050	200 ± 170	230 ± 140	-120 ± 140	-120 ± 150
1100	180 ± 190	210 ± 150	-80 ± 150	-80 ± 150
1150	160 ± 170	190 ± 140	-20 ± 140	-20 ± 140
1200	150 ± 140	180 ± 130	40 ± 130	40 ± 140
1250	120 ± 130	150 ± 110	90 ± 110	100 ± 140

dramatically, and XRD will readily detect decreases in the lattice parameter due to absorption of boron into the silicon crystal lattice, as previously discussed. Excess boron, which had previously precipitated, forming either boron interstitial clusters or silicon boride, dissolves and occupies substitutional sites within the silicon lattice, thereby decreasing the lattice parameter, according to Vegard's law.

The diffusion of boron within silicon occurs relatively quickly, allowing for the solubility limit to be achieved within the first few seconds of reaching the equilibrium temperature. Indeed, the semiconductor industry anneals heavily boron-doped silicon in a matter of milliseconds to achieve this substitutional effect.³⁸ For this reason, even with the relatively fast acquisition rate afforded by synchrotron radiation, the active boron substitution is difficult to observe as the equilibrium state is rapidly attained. Cooling the material at the relatively slow rate of 100°C/min also has the effect of re-precipitating the excess boron greater than the solubility limit back out of the silicon as either silicon boride or boron clusters.³⁹ Therefore, the boron concentration is found as a relatively smooth function of temperature in the XRD data.

By incorporating Equation (15) into the residual strain formulation, the residual strain within the silicon now exhibits the expected relaxation trend. This is seen in Figure 8 as the thick

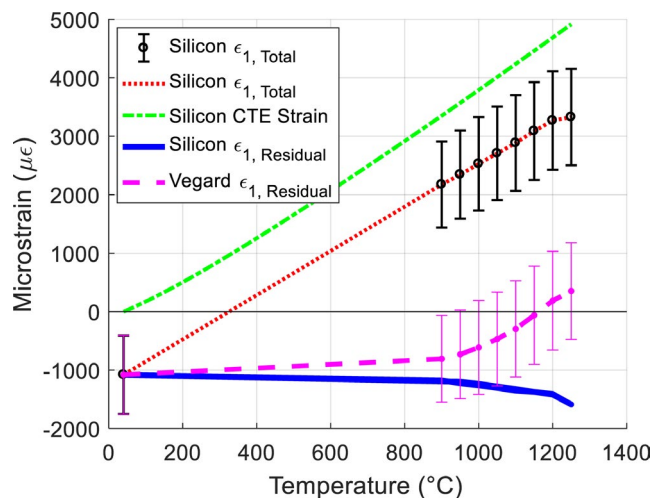


FIGURE 8 The silicon crystallite strain state ϵ_1 in the fiber weft direction through heat treatment is shown by open circles, with error bars denoting strain standard deviation. The dashed CTE strain line represents expected strain due to thermal expansion effects as a function of temperature. The solid $\epsilon_{1,Residual}$ line represents the difference of these two, while the $\epsilon_{1,Vegard}$ dashed line accounts for the increase in lattice parameter due to additional boron dissolving with rising temperature. Error bars on the $\epsilon_{1,Vegard}$ line represent a combination of X-ray diffraction standard deviations and published CTE standard deviations.²⁸ These two lines represent the bounds of the residual strain in the studied silicon as a function of temperature. As temperatures decreased back to room temperature, the silicon strain states returned to approximately the same levels [Color figure can be viewed at wileyonlinelibrary.com]

dashed line. These corrections may now overestimate the effects of boron solubility and silicon lattice contraction, as the strains estimated by these corrections become tensile around 1200°C. However, the additional stress-producing mechanisms found within the manufacture of the CMC (eg, CVI and slurry infiltration) add ambiguity as to what the stress-free temperatures are for each constituent. It can be said the two thick solid and dashed “Residual” lines are bounds for the true residual strain state, though the true stresses are likely closer to the corrected line, as previous research has shown localized substitutional (in the form of activated) boron concentrations near the maximum phase-diagram concentrations developed by Armigliato et al.^{4,14,35} Therefore, the strains and stresses associated with these temperatures provide both a qualitative and quantitative understanding of the many mechanisms at work within this composite system. Table 4 presents mean residual stress data (corrected for both CTE and maximum boron solubility) through heat treatment, utilizing the corrected strains and the constitutive relationship developed previously.

An ANOVA was performed on the total strain data for silicon and also resulted in exceptionally low p-values. Performing pairwise comparisons, each change in temperature of at least 150°C resulted in a statistically significant change in total strain, the highest p-value being between 900°C and 1050°C ($P = .014$). Therefore, we can again say that the total strain shows temperature dependence. For the case of residual strain, we performed an ANOVA and when comparing strain at adjacent 50°C increments, there is no statistically significant change in the residual strain state. However, temperature differences of 200°C or more (residual strains at 40°C notwithstanding) resulted in statistically significant changes to the residual strain, while pairwise strain comparisons between 40°C and 1000°C and greater also differed at statistically relevant levels.

The transmission XRD technique used herein provides a measure of constituent-scale residual stress in SiC/SiC CMC materials that is complimentary to alternative methods found in literature. For example, the balance in stress between the silicon and SiC phases of the matrix results in a volume average stress that is similar to measurements reported using the CIP^{7,40,41} and material removal methods.⁴² In a previous study, Raman spectroscopy was used to measure residual hydrostatic stresses of approximately 240–340 MPa in the silicon phase of material with similar pedigree to that used in the current study.¹⁴ These results are in agreement with those reported in the current work for both the SiC and the silicon phases of the matrix material.

5 | CONCLUSIONS

In situ residual strain measurements through heat-treatment cycles showed little change in residual stress in the silicon

carbide particles through heat treatment. As expected, the residual strain within silicon carbide particles was observed to decrease as a function of temperature. The same in situ measurements showed that the residual strain within the silicon became more compressive if only the CTE of silicon was considered. Investigating further, the solubility of boron within silicon greatly increases with increasing temperature, and applying the relationships of how this affects the silicon lattice parameter, the magnitude of residual silicon strain was shown to decrease with increasing temperature. Although the residual silicon strains at very high temperatures were determined to become tensile, the tensile determination was made using many assumptions over very large temperature ranges and the conclusions should be taken in a qualitative, rather than a quantitative manner. To fully understand the changes in silicon strain with respect to temperature, additional experimental methods are necessary to determine the boron concentrations. The known boron concentrations could then be used to deconvolve the strains found using Vegard's law and the residual strains of the silicon.

ACKNOWLEDGMENTS

This research used resources of the Advanced Photon Source, a US Department of Energy (DOE) Office of Science User Facility operated for the DOE Office of Science by Argonne National Laboratory under contract no. DE-AC02-06CH11357.

OWNERSHIP

The authors declare that the submitted work is our own and that copyright has not been breached in seeking publication. The authors declare that the submitted work has not previously been published in full, and is not being considered for publication elsewhere.

ORCID

Michael W. Knauf  <https://orcid.org/0000-0003-1418-5651>

Paul A. Shade  <https://orcid.org/0000-0002-7516-4275>

REFERENCES

1. Wing B, Esmonde-White F, Halloran J. Microstress in reaction-bonded SiC from crystallization expansion of silicon. *J Am Ceram Soc.* 2016;99(11):3705–11.
2. Wing B, Halloran J. Relaxation of residual microstress in reaction bonded silicon carbide. *Ceram Int.* 2018;44(10):11745–50.
3. Zhang X, Zhang T, Wong M, Zohar Y. Effects of high-temperature rapid thermal annealing on the residual stress of LPCVD-polysilicon thin films. *Proceedings of the Tenth Annual Workshop on Micro Electro Mechanical Systems, IEEE;* 1997 Jan 26–30; Nagoya, Japan. *IEEE.* 1997:535–40.
4. Knauf M, Przybyla C, Ritchey A, Trice R, Pipes RB. Residual stress determination of silicon containing boron dopants in CMCs. *J Am Ceram Soc.* 2019;102(5):2820–9.
5. Agaiby R, Becker M, Thapa S, Urmoneit U, Berger A, Gawlik A, et al. Stress and doping uniformity of laser crystallized amorphous silicon in thin film silicon solar cells. *J Appl Phys.* 2010;107(5):054312.
6. Mei H. Measurement and calculation of thermal residual stress in fiber reinforced ceramic matrix composites. *Compos Sci Technol.* 2008;68(15):3285–92.
7. Dassios K, Matikas T. Residual stress-related common intersection points in the mechanical behavior of ceramic matrix composites undergoing cyclic loading. *Exp Mech.* 2013;53:1033–8.
8. Morscher G, Gordon N. Acoustic emission and electrical resistance in SiC-based laminate ceramic composites tested under tensile loading. *J Eur Ceram Soc.* 2017;37(13):3861–72.
9. Bobet J, Lamon J. Study of thermal residual stresses in ceramic matrix composites. *J Alloys Compd.* 1997;259:260–4.
10. Bobet J, Lamon J. Thermal residual stresses in ceramic matrix composites-I: axisymmetrical model and finite element analysis. *Acta Metall Mater.* 1995;43(6):2241–53.
11. Bobet J, Naslain R, Guette A, Ji N, Lebrun J. Thermal residual stresses in ceramic matrix composites-II: experimental results for model materials. *Acta Metall Mater.* 1995;43(6):2255–68.
12. Harder B, Almer J, Weyant C, Lee K, Faber K. Residual stress analysis of multilayer environmental barrier coatings. *J Am Ceram Soc.* 2009;92(2):452–9.
13. Ramirez-Rico J, Stolzenburg F, Almer J, Routbort J, Singh D, Faber K. In situ imaging and strain determination during fracture in a SiC/SiC ceramic matrix composite. *Scr Mater.* 2013;69(7):497–500.
14. Knauf M, Przybyla C, Ritchey A, Trice R, Pipes RB. Measuring the effects of heat treatment on SiC/SiC ceramic matrix composites using Raman spectroscopy. *J Am Ceram Soc.* 2020;103(2):1293–303.
15. Park J, Okansinski J, Chatterjee K, Chen Y, Almer J. Non-destructive characterization of engineering materials using high-energy X-rays at the Advanced Photon Source. *Synchrotron Radiat News.* 2017;30(3):9–16.
16. Kaiser D, Watters J. *Standard Reference Material 674b; X-Ray Powder Diffraction Intensity Set for Quantitative Analysis by X-Ray Powder Diffraction.* Gaithersburg, MD: NIST; 2007.
17. Reed-Hill RE. *Physical metallurgy principles.* Boston, MA: PWS-KENT; 1992.
18. Shinavski R. Enhanced strength nanolayered SiC for micro gas turbine power generation. Huntington Beach, CA: Hyper-Therm High-Temperature Composites, Inc.; 2002. p. 53.
19. Withers P, Bhadeshia H. Residual stress, part 1—measurement techniques. *Compos Sci Technol.* 2001;17:355–64.
20. Haeffner D, Almer J, Lienert U. The use of high energy X-rays from the Advanced Photon Source to study stresses in materials. *Mater Sci Eng A.* 2005;399(1-2):120–7.
21. Munro R. Material properties of a sintered a-SiC. *J Phys Chem Ref Data.* 1997;26(5):1195–203.
22. Slack G, Bartram S. Thermal expansion of some diamondlike crystals. *J Appl Phys.* 1975;46(1):89–98.
23. Li Z, Bradt R. Thermal expansion of the hexagonal (6H) polytype of silicon carbide. *J Am Ceram Soc.* 1986;69(12):863–6.
24. Inoue Z, Kurachi Y. Structure change of SiC at high temperature. In: Somiya S, (Ed.). *Proceedings of the International Symposium on Ceramic Components for Engines;* 1983 Oct 17–19; Hakone, Japan. Tokyo, Japan: KTK Scientific Publisher; 1983. p. 519–27.
25. Hopcroft M, Nix W, Kenny T. What is the Young's modulus of silicon? *J Microelectromech Syst.* 2010;19(2):229–38.

26. Ono N, Kitamura K, Nakajima K, Simanuki Y. Measurement of Young's modulus of silicon single crystal at high temperature and its dependency on boron concentration using the flexural vibration method. *Jpn J Appl Phys.* 2000;39(2R):368–71.
27. Swarnakar A, Van der Biest O, Vanhellefont J. Determination of the Si Young's modulus between room and melt temperature using the impulse excitation technique. *Phys Status Solidi C.* 2014;11(1):150–5.
28. Okada Y, Tokumaru Y. Precise determination of lattice parameter and thermal expansion coefficient of silicon between 300 and 1500K. *J Appl Phys.* 1984;56(2):314–20.
29. Suyama S, Kameda T, Itoh Y. Effect of structure of interfacial coating layer on mechanical properties of continuous fiber reinforced reaction sintered silicon carbide matrix composite. *J Mater Sci.* 2002;37(6):1101–6.
30. Vegard L. Die Konstitution der Mischkristalle und die Raumfüllung der Atome. *Z Phys.* 1921;5(1):17–26.
31. Okada Y. Diamond cubic Si: structure, lattice parameter, and density. In R Hull, editor. *Properties of crystalline silicon.* London, UK: INSPEC, 1999;20:p. 91–7.
32. Celotti G, Nobili D, Ostoia P. Lattice parameter study of silicon uniformly doped with boron and phosphorus. *J Mater Sci.* 1974;9:821–8.
33. Holloway H, McCarthy S. Determination of the lattice contraction of boron-doped silicon. *J Appl Phys.* 1993;73(1):103–11.
34. Becker P, Bettin H, Danzebrink H, Gläser M, Kuetgens U, Nicolaus A, et al. Determination of the Avogadro constant via the silicon route. *Metrologia.* 2003;40(5):271.
35. Armigliato A, Nobili D, Ostoja P, Servidori M, Solmi S. Solubility and precipitation of boron in silicon and supersaturation resulting by thermal predeposition. In: Huff H, Sirtl E, editors. *Semiconductor silicon.* Princeton, NJ: Electrochemical Society; 1977. p. 638–47.
36. Hauk V, ed. *Structural and residual stress analysis by nondestructive methods: evaluation-application-assessment.* Amsterdam: Elsevier. 1997.
37. Olesinski R, Abbaschian G. The B–Si (boron-silicon) system. *J Phase Equilib.* 1984;5(5):478–84.
38. Skorupa W, Yankov R, Anwand W, Voelskow M, Gebel T, Downey D, et al. Ultra-shallow junctions produced by plasma doping and flash lamp annealing. *Mater Sci Eng B.* 2004;114:358–61.
39. Salvador D, Napolitani E, Bisognin G, Carnera A, Bruno E, Mirabella S, et al. Dissolution kinetics of B clusters in crystalline Si. *Mater Sci Eng B.* 2005;124:32–8.
40. Morscher G, Baker C, Smith C. Electrical resistance of SiC fiber reinforced SiC/Si matrix composites at room temperature during tensile testing. *Int J Appl Ceram Technol.* 2014;11(2):263–72.
41. Morscher G. Stress dependent matrix cracking in 2D woven SiC-fiber reinforced melt-infiltrated SiC matrix composites. *Compos Sci Technol.* 2004;64(9):1311–9.
42. Beyerle D, Spearing S, Evans A. Damage mechanisms and the mechanical properties of a laminated 0/90 ceramic/matrix composite. *J Am Ceram Soc.* 1992;75(12):3321–30.

How to cite this article: Knauf MW, Przybyla CP, Shade PA, et al. In situ characterization of residual stress evolution during heat treatment of SiC/SiC ceramic matrix composites using high-energy X-ray diffraction. *J Am Ceram Soc* 2021;104:1424–1435. <https://doi.org/10.1111/jace.17493>